Supplementary Information for

Realizing thermoelectric conversion efficiency of 10% with long-term stability in kesterite $Cu_2ZnSn(S_{1-x}Se_x)_4$ single-leg device

Akira Nagaoka[a, b]*, Shoma Miura[c], Keita Nomoto[d], Kangwei Chen[d], Naoki Sato[e], Kenji Yoshino[a, b], and Kensuke Nishioka[a, b]

[a]Electrical and Electronic System Program, University of Miyazaki, Miyazaki 889-2192, Japan
[b]GX Research Center, University of Miyazaki, Miyazaki 889-2192, Japan
[c]Graduate School of Engineering, University of Miyazaki, Miyazaki 889-2192, Japan
[d]School of Aerospace, Mechanical and Mechatronic Engineering and Australian Centre for Microscopy and Microanalysis, The University of Sydney, Sydney, 2006, Australia
[e]Research Center for Materials Nanoarchitectonics (MANA), National Institute for Materials Science (NIMS), Ibaraki 305-0044, Japan

*Corresponding author: nagaoka.akira.m0@cc.miyazaki-u.ac.jp

Single crystal growth by Traveling Heater Method (THM):

It is generally difficult to grow high-quality $Cu_2ZnSn(S_{1-x}Se_x)_4$ (CZTSSe) single crystals from melt because this material grows through a peritectic reaction as liquid phase + ZnS (or ZnSe) solid phase [S1, S2]. On the other hand, growth by the THM based on solution growth, which can proceed below the melting point, is well-suited for high-quality CZTSSe single crystals.

Feed polycrystalline of CZTSSe was synthesized by using a melting reaction. Cu (99.999%), Zn (99.9999%), Sn (99.9999%), S (99.999%), and Se (99.999%) shots and Na_2S (99%) powder were used as starting materials. Prior to growth, Cu, Zn, and Sn were chemically etched with HCl solution for 60 s and then rinsed in ultrapure 18MOhm water. The ingots (15 g) with nominal compositions were synthesized by mixing the described amounts of elements in a carbon-coated 2 mm wall thickness quartz ampoule with 9 mm inner diameter under high vacuum of 10^{-4} Pa and then flame-sealed off. In a vertical furnace, the sealed ampoule was heated at 200 ºC/h to 650 ºC and held at this temperature for 24 h to react the constituents and prevent explosion from the chalcogen overpressure. Then the sealed ampoule was heated at 80 ºC/h to 1100 ºC and held at this temperature for 24 h to complete the reaction and ensure homogenization. The ampoule was then removed from the furnace and allowed to cool rapidly in air.

The feed polycrystalline CZTSSe ingot (80 mol%) and Sn solvent (20 mol%) were loaded into a carbon-coated 2 mm wall thickness quartz ampoule with 10 mm inner diameter. The ampoule was flame-sealed off under high vacuum of 10^{-4} Pa, and then inserted into the THM furnace. The THM furnace has three coil heaters (upper, main, and bottom) for controlling temperature gradient. The upper heater temperature of 850 ºC was used to prevent a sulfur (or selenium) deficiency in the grown CZTSSe crystal. The sulfur species evaporated from liquid zone condensed on the cold wall of the ampoule without heating the upper part, thereby reducing the sulfur mole fraction in the crystal. For the THM growth, the main heater temperature (growth

temperature) was 900 ºC which is 50 ºC higher than liquids temperature, and temperature gradient between the main and bottom heaters (the supersaturation region for single crystal growth) was about 40 ºC/cm. This temperature gradient can control the length of solution zone. The growth speed was 4-5 mm/day for 10 days. CZTSSe single crystals were cooled at the rate of 600 ºC/h from 700 ºC after crystal growth. The dimensions of single crystal ingot are 10 mm in diameter and 40 mm length including zone solution region.

Characterization

Structural properties

The combination of X-ray diffraction (XRD) and Raman spectroscopy is a useful tool for investigation of secondary phases because the XRD peaks of CZTSSe overlap well with those of Cu_2S (Cu_2Se) and ZnS (ZnSe), especially. The result details of both measurements are reported in our previous papers [S3, S4]. The powder XRD pattern of each composition of samples exhibits major peaks corresponding to diffraction lines of the kesterite structure of Cu_2ZnSnS_4 (CZTS; ICDD data #00-026-0575) and $Cu_2ZnSnSe_4$ (CZTSe; ICDD data #00-052-0868) in Fig. S1A. The distinct peak at around 2θ = 18.3º can be observed for distinguishing between the kesterite and stannite structures. Samples in this study have the kesterite structure without secondary phases from XRD measurement. No secondary phases, such as Cu_2SnS_3, Cu_2Se and ZnS (ZnSe) were observed in Raman measurement by 532 nm excitation source, as shown in Fig. S1B. The spectra show clear the peaks of CZTS at 287, 338 and 353 cm^{-1}, while those of CZTSe at 170, 193 and 231 cm^{-1}. Raman peaks clearly shift toward the low frequency region to being proportional to the increasing of Se composition values x.

The crystal quality of CZTSSe single crystals for TE measurements were evaluated by X-ray rocking curve (XRC) method shown in Fig. S2. It can be observed that the curves have good

symmetry and narrow full width at half-maximum (FWHM). The results of multi-point tests on different positions of the sample wafer show that the FWHM of the (004) diffraction peak is between 120 to 142 arcsec, which means that the crystal integrity of samples 1-5 is quite good. The [001] crystallographic orientation of all samples can be observed by scanning electron microscope (SEM) with electron backscatter diffraction (EBSD) in Fig. S3.

Pseudo-cubic structure

The tetragonal kesterite structure is analogous to a 1 × 1 × 2 supercell expansion of the zinc-blende structure which represents the pseudo-cubic approach in Fig. S4A. A non-cubic structure can easily achieve low symmetry with crystal-field splitting ΔCF, which implies low degenerate band-edge electronic states. The value of ΔCF could be tuned to 0 when the crystal structure parameter $c/2a$ was equal to 1, where c and a are lattice parameters for kesterite, leading to a pseudo-cubic structure. Figure S4B shows the observation of pseudo-cubic structure in sample 2 from the scanning transmission electron microscopy (STEM)-High-angle annular dark-field (HAADF) image, which the crystal structure parameter $c/2a = 0.995$ ($a = 0.546$ nm and $c = 1.087$ nm) minimizes the energy splitting parameter ΔCF.

Degree of order in CZTSSe

The degree of order in CZTSSe samples must be determined for a comprehensive study. Limited by the dynamic nature of cooling from the growth temperature, the CZTSSe lattice relaxed to a Cu/Zn antisite random state (disordered structure) owing to the similar atomic numbers and sizes of Cu and Zn. A remarkably low cooling rate (~100 °C/h) was adopted in our previous study [S5] for the ordered kesterite CZTS structure based on the Raman intensity ratio. However, this

strategy cannot be applied to CZTSe and CZTSSe because their Raman intensity ratios change negligibly even under multiwavelength excitation [S6]. Recently, the temperature dependence of Seebeck coefficient *S* has been suggested as a probe for the order–disorder transition because different cooling-rate-dependent tendencies can be observed [S7]. Considering the impact of the order–disorder transition on thermoelectric (TE) properties, the temperature dependences of *S* for CZTSSe single crystals (Sample 1; x = 0.2 and Sample 3; 0.8) were monitored at different cooling rates from the growth temperature in Figs. 5A-B. Ordered and disordered states were obtained via slow (10 °C/h) and rapid cooling (600 °C/h), respectively, immediately from 700 °C after crystal growth. Obvious differences were noted in the slopes for both samples in the 500–600 K and 450–550 K ranges, respectively, near their critical transition temperatures (533 K for CZTS [S5, S7] and 473 K for CZTSe [S8]). Additionally, the temperature dependence of specific heat C_p of the stoichiometric samples at different cooling rates was investigated (Figs. 5C-D). The C_p values of the disordered samples increased monotonically with increasing temperature, according to the Dulong–Petit law, whereas those of the ordered samples showed a small decrease near their respective critical transition temperatures, which is consistent with the Seebeck-coefficient-related results. The mass of all samples is unchanged after measurements by using Thermogravimetric analysis (TGA) (Fig. S6).

Compositional properties

The detailed compositional results of each sample determined by inductively coupled plasma-atomic emission spectroscopy (ICP-AES) are shown in Table S1. In this study, our strategy for improvement of TE properties is the utilization of shallower Cu vacancy (V_{Cu}) acceptor by Cu-poor, Zn-rich condition than Cu on Zn antisite (Cu_{Zn}) for reported quaternary compounds by Cu-

rich, Zn-poor condition. In addition, the concentration of unintentional impurities detected by ICP-AES is summarized in Table S2, for which the effect of K-doping is confirmed. The unintentional impurity concentrations are fairly low (less than several hundreds of ppb level).

Thermoelectric conversion efficiency

TE conversion efficiency (η) can be determined by the equation (s1);

$$\eta = \frac{P}{Q_{in}} = \frac{P}{P + Q_{out} + Q_{rad}} \qquad (s1)$$

where P, Q_{in}, Q_{out}, and Q_{rad} are generated power, input power from hot side, heat flow out of cold side, and radiation loss from the single-leg, respectively. The direct measurement of Q_{in} is of great challenge due to the heavy heat loss at high temperature. The total Q_{in} includes P, Q_{out}, and Q_{rad}. Considering the minimization of radiation loss from the sides of the single-leg, the samples were cut for a small length of ~ 5 mm and it was well polished to increase the heat flow in this study. The heat radiation loss can be ignored in this study, which is typical determination of η values for reported TE single-legs [S9, S10]. In addition, the heat radiation loss as much as 5% of total heat flow can be estimated by finite difference method [S11]. Thus, the conversion efficiency formula is reduced to equation (s2).

$$\eta = \frac{P}{Q_{in}} = \frac{P}{P + Q_{out}} \qquad (s2)$$

The conversion efficiency of CZTSSe single-leg can be calculated by equation (s2) in this study.

Aging test conditions and stability evaluation

The long-term stability of CZTSSe single-leg TE device was evaluated through aging tests conducted for over 1000 h. To ensure consistency, all tests were performed on the same device,

with measurements taken after various aging durations. The device was sealed in a quartz ampoule under high vacuum (~10^{-4} Pa) and subjected to thermal aging at 800 K with a heating rate of 200 K/h in a furnace. After each designated aging interval, the sealed ampoule was rapidly cooled in air, and the device was removed to measure its TE conversion efficiency under a temperature difference of 473 K. Following TE efficiency measurement, the device was vacuum-sealed again and subjected to the next aging cycle. The conversion efficiency of the CZTSSe-based single-leg TE device was evaluated by measuring electrical output power and output heat flow under vacuum (~10^{-2} Pa) using an M612-B tester (MOTTAINAI ENERGY).

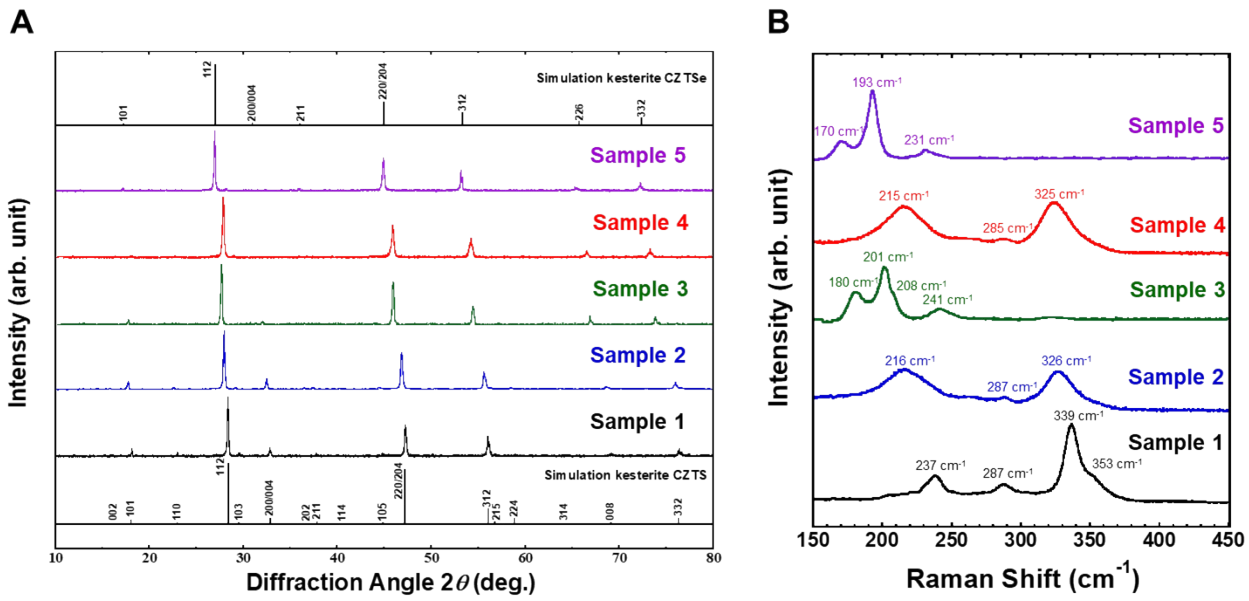

Figure S1. Structural properties for various compositional CZTSSe samples for confirming of kesterite phase by (**A**) the powder XRD patterns and (**B**) Raman spectroscopy.

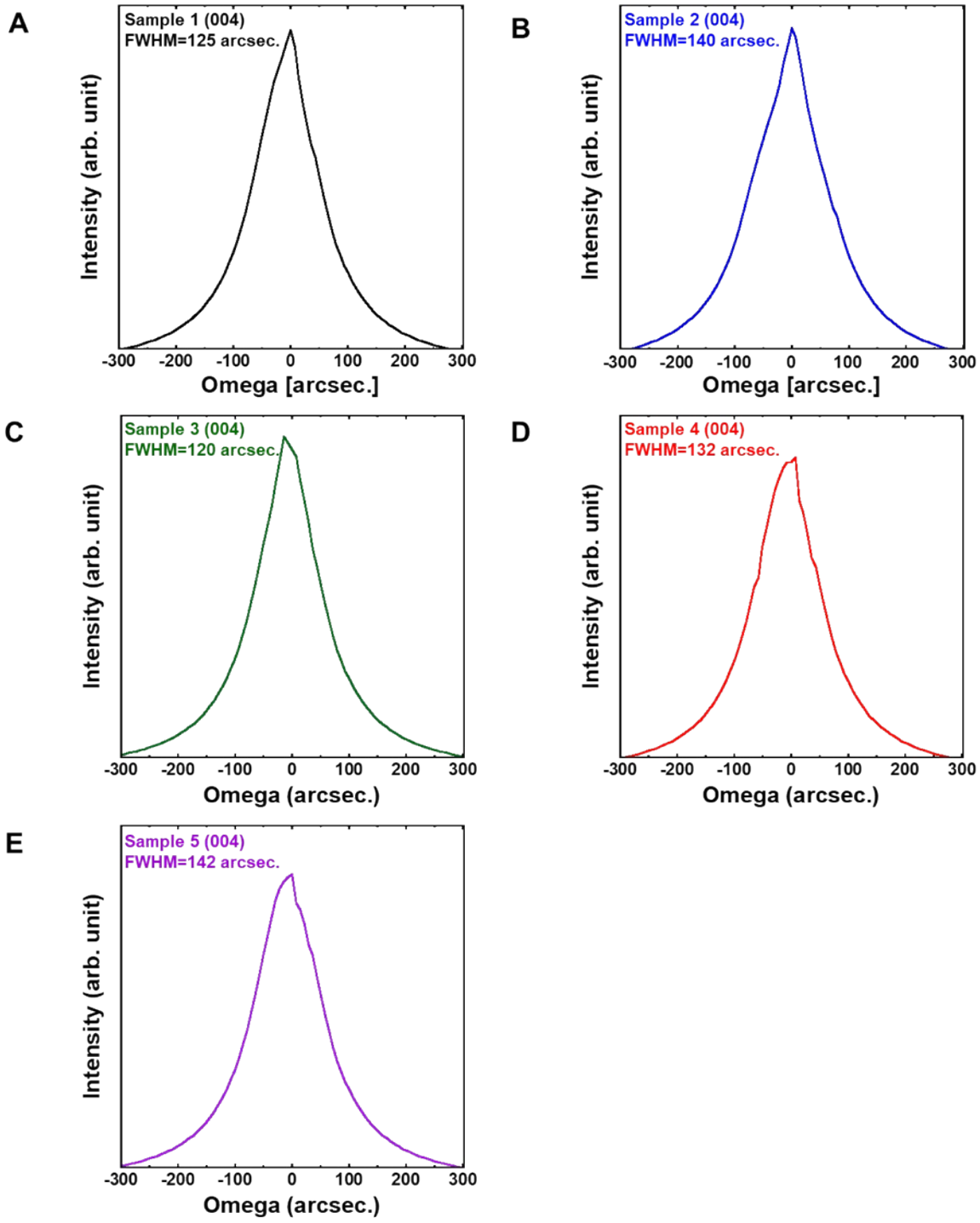

Figure S2. XRC results of CZTSSe (004) wafers for crystal quality. (**A**) Sample 1 (x = 0.2), (**B**) sample 2 (x = 0.5), (**C**) sample 3 (x = 0.8), (**D**) sample 4 (x = 0.5 and K-doped) and (**E**) sample 5 (x = 1 and K-doped).

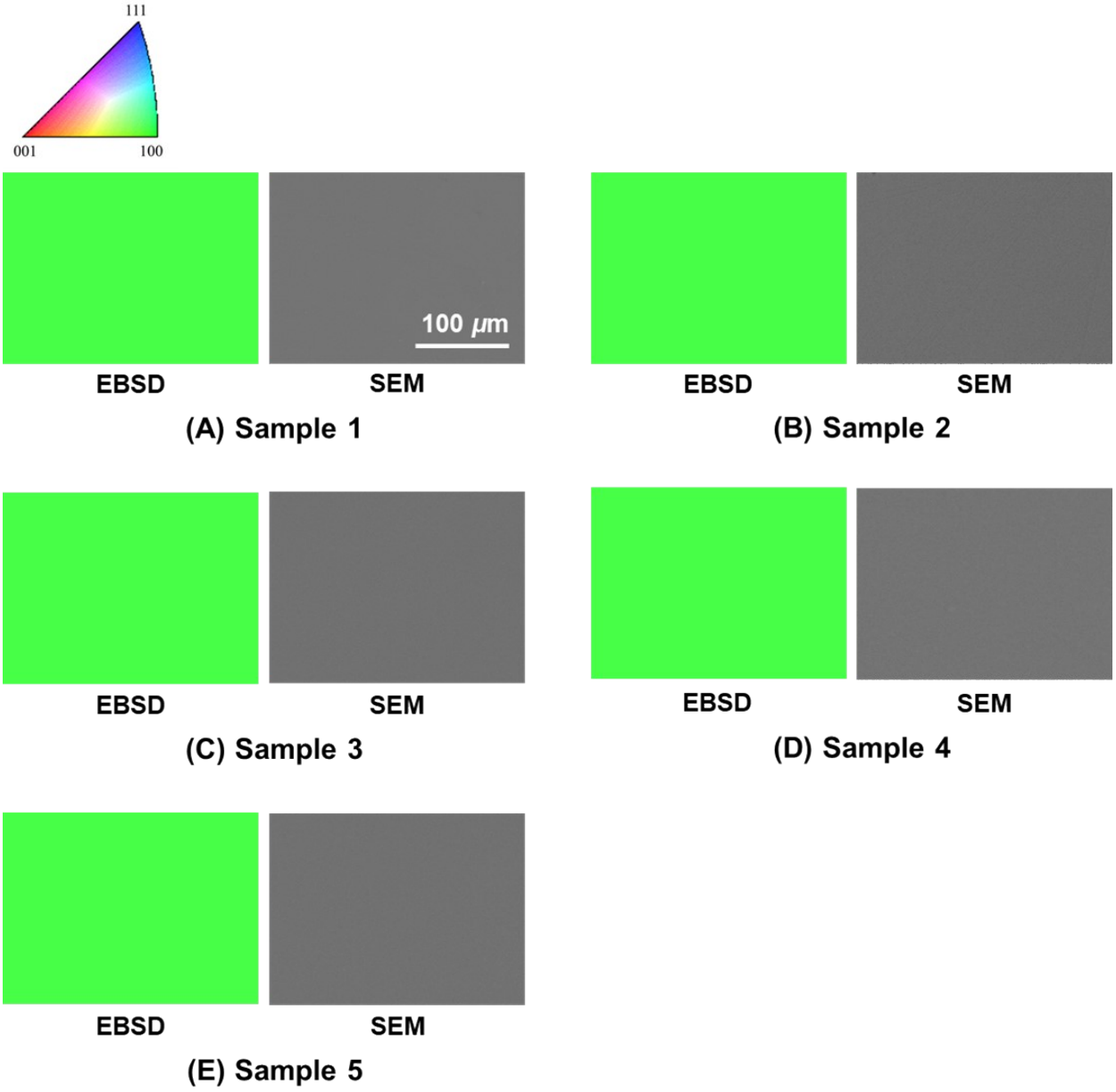

Figure S3. The Observation of [001] crystallographic orientation of CZTSSe samples 1-5 by EBSD images. (**A**) Sample 1 (x = 0.2), (**B**) sample 2 (x = 0.5), (**C**) sample 3 (x = 0.8), (**D**) sample 4 (x = 0.5 and K-doped) and (**E**) sample 5 (x = 1 and K-doped).

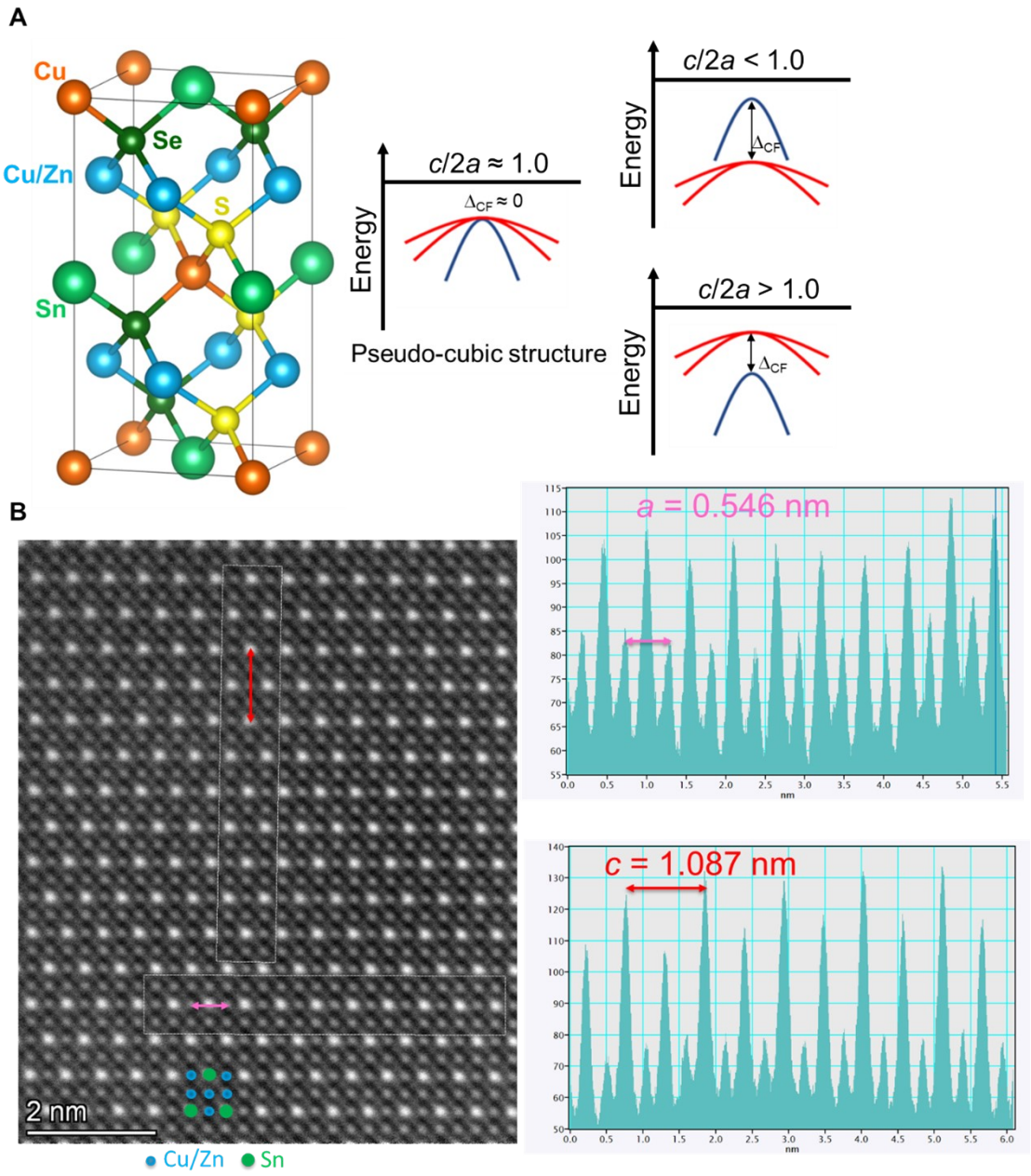

Figure S4. (**A**) Pseudo-cubic approach of Cu/Zn disordered structure for CZTSSe. The crystal-field splitting ΔCF depends on the crystal structure parameter *c*/2*a*. (**B**) The STEM-HAADF image shows the pseudo-cubic structure of CZTSSe single crystal (sample 2) on an atomic scale along [100] zone axis. The blue and green dots marked on the atomic columns represent Cu/Zn and Sn atoms, respectively. The line profiles of the Cu/Zn contrast (purple double arrow) and Sn contrast (red double arrow) show the unit cell parameters *a* and *c*, respectively.

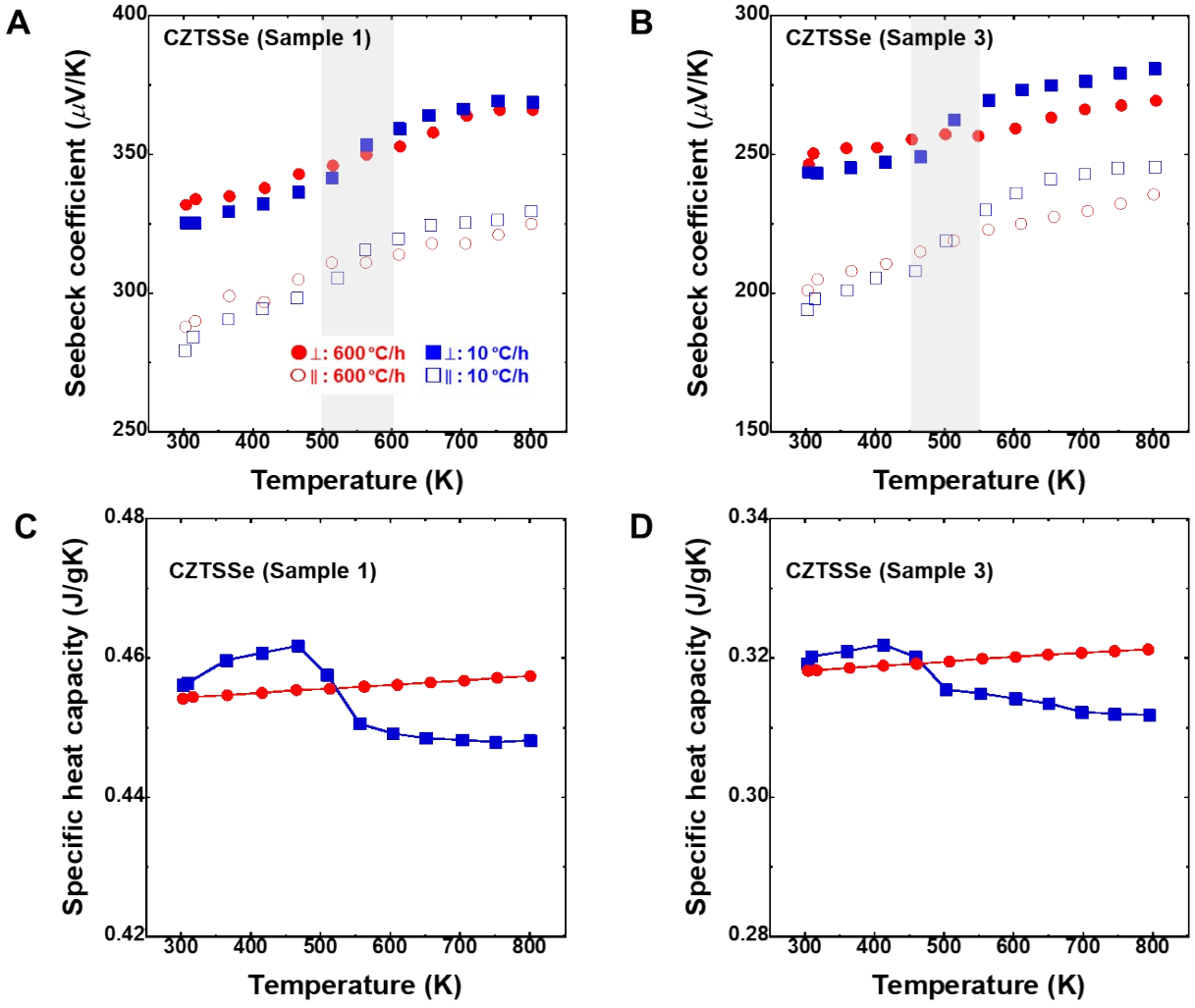

Figure S5. The observation of ordered-disordered transition in CZTSSe single crystals. Temperature dependence of (**A, B**)Seebeck coefficient *S* for samples with different cooling rate and (**C, D**) specific heat capacity C_p. The slopes for Seebeck coefficient of both samples were different between 500 K to 600 K and 450 K to 550 K (gray region) near critical transition temperatures of 533 K (CZTS) and 473 K (CZTSe).

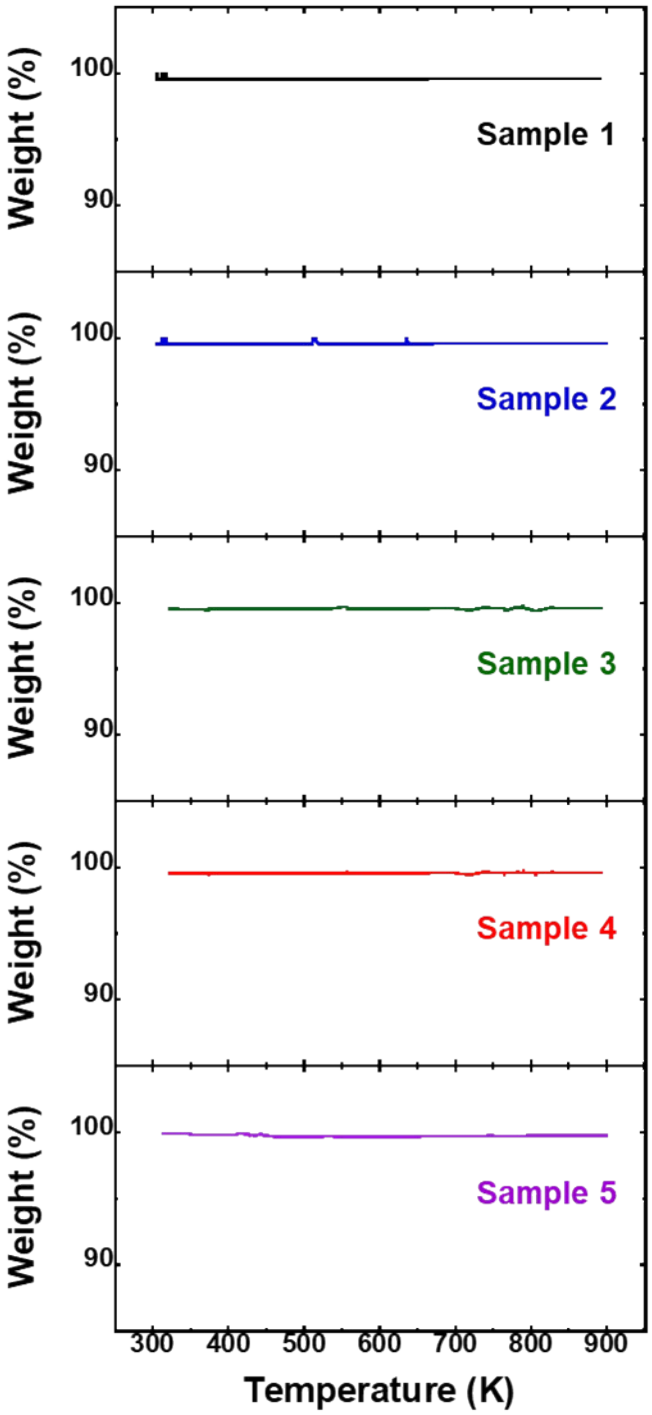

Figure S6. The TGA measurements of samples 1-5. All samples are stable at the temperature up to 900 K in N_2 atmosphere.

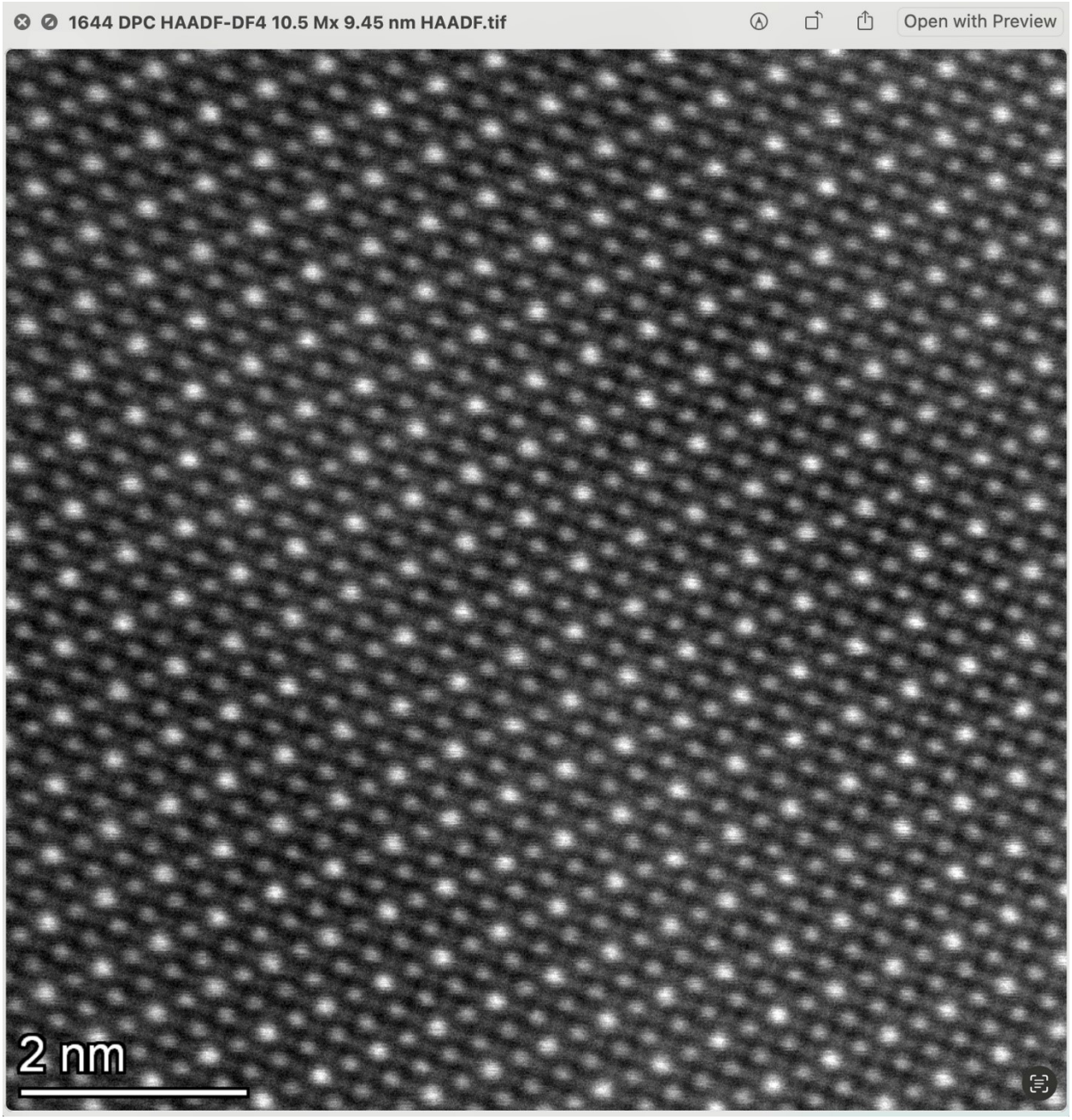

Figure S7. TEM high-angle annular dark-field (STEM-HAADF) image of CZTSSe single crystal (sample 4) along [100] zone axis.

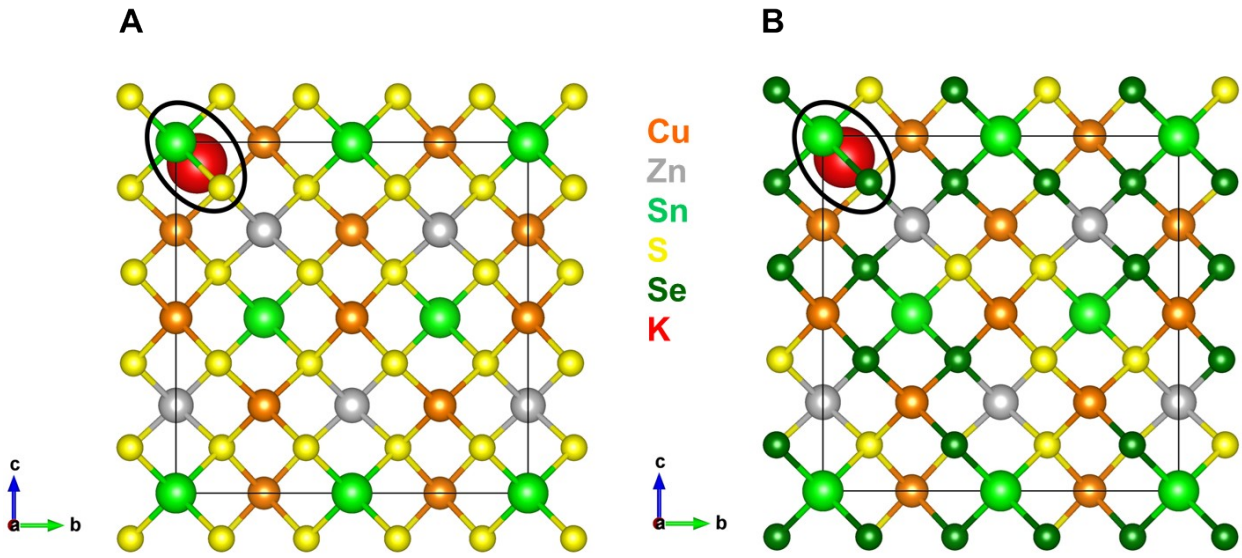

Figure S8. Supercell crystal structures for DFT calculation. K-doped (**A**) Cu_2ZnSnS_4 (CZTS) and (**B**) CZTSSe. To reproduce the experimentally observed K atom positions near Sn atoms, a K atom was introduced into an interstitial site in a 2×2×1 supercell.

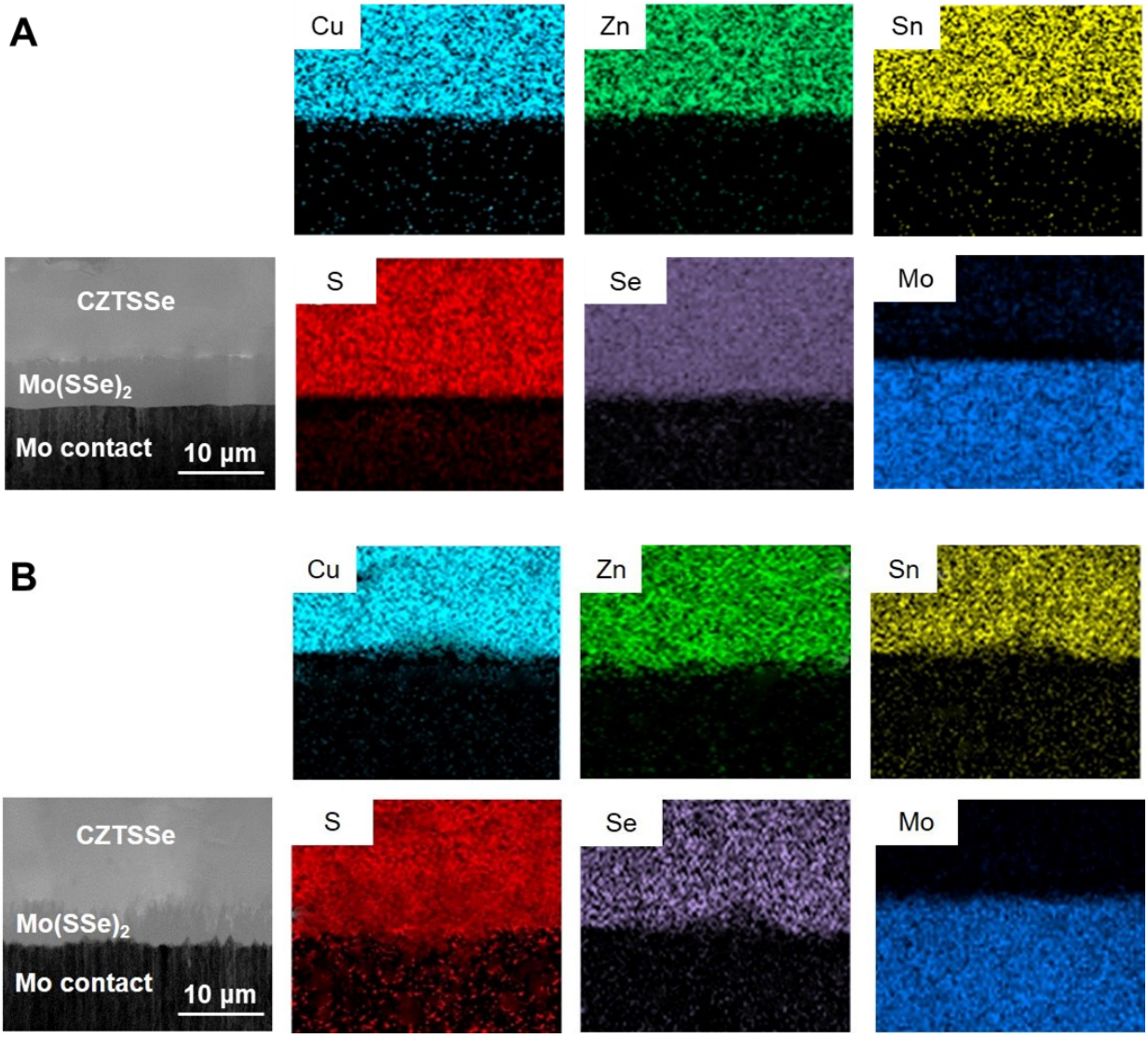

Figure S9. Compositional mapping measurements by energy dispersive X-ray spectroscopy (EDX) for CZTSSe/$Mo(SSe)_2$/Mo interfaces (**A**) before and (**B**) after aging test for 1100 h at 800 K.

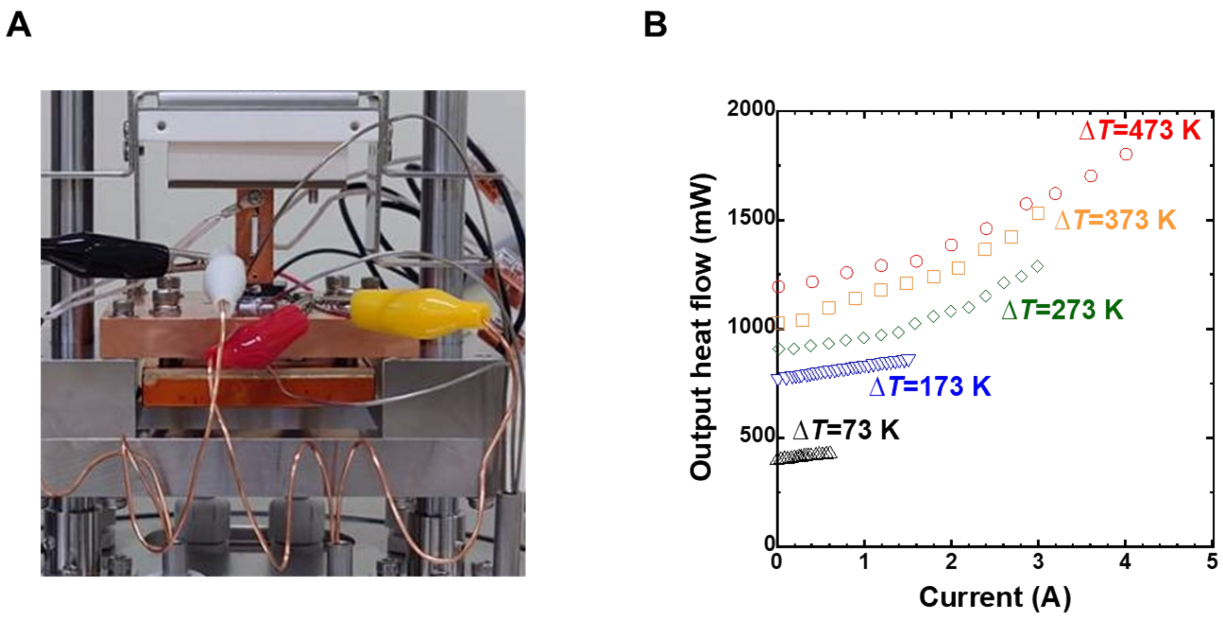

Figure S10. (**A**) Photograph of CZTSSe-based single-leg mounted on measurement system. (**B**) Current dependence of output heat flow under different temperature gradients (ΔT).

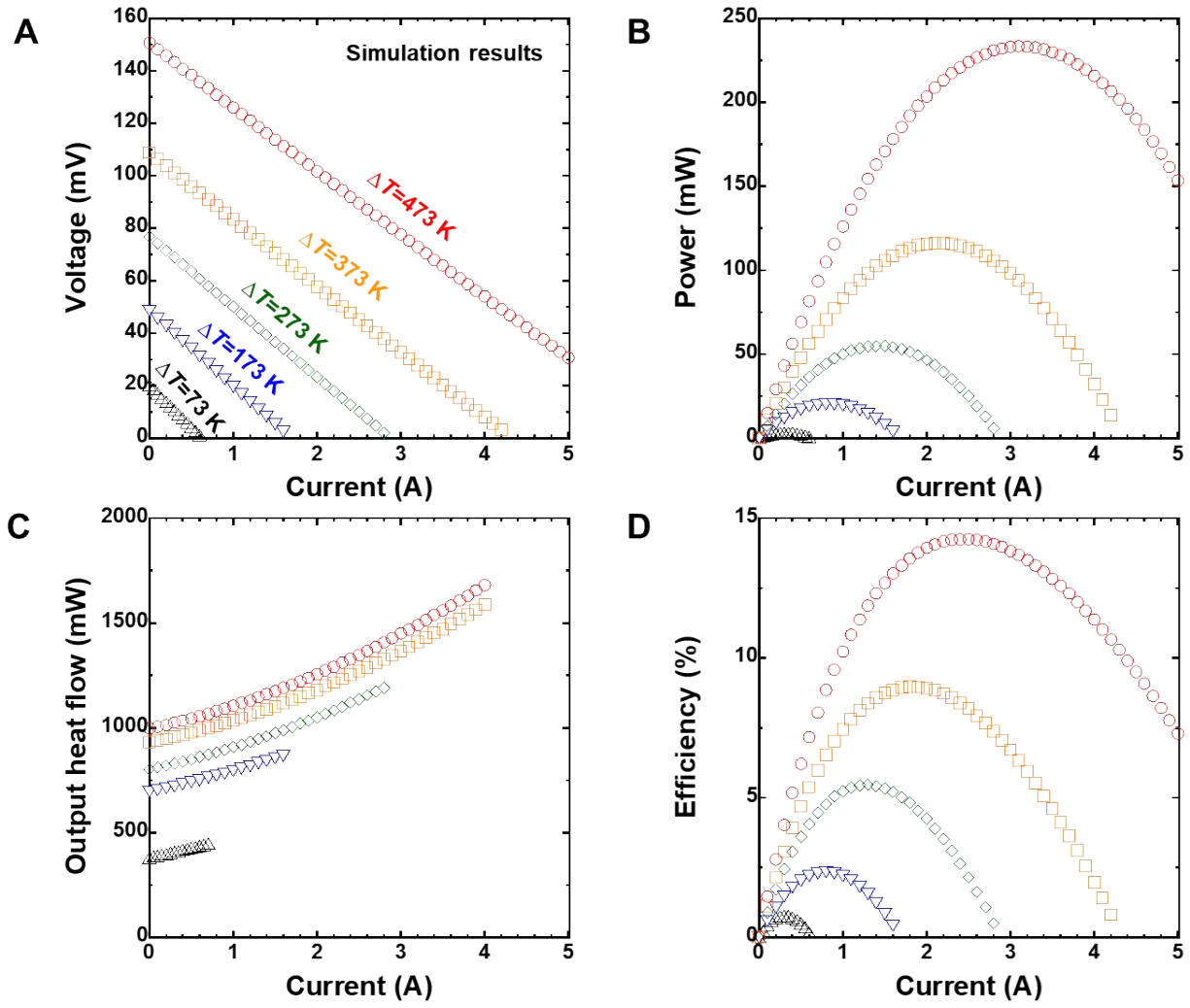

Figure S11. Simulation results of CZTSSe-based single-leg TE device obtained through COMSOL. (**A**) Output voltage (V), (**B**) output power (P), (**C**) output heat flow from the cold-side (Q_{out}), and (**D**) conversion efficiency (η) as a function of current (I) under various temperature gradients (ΔT).

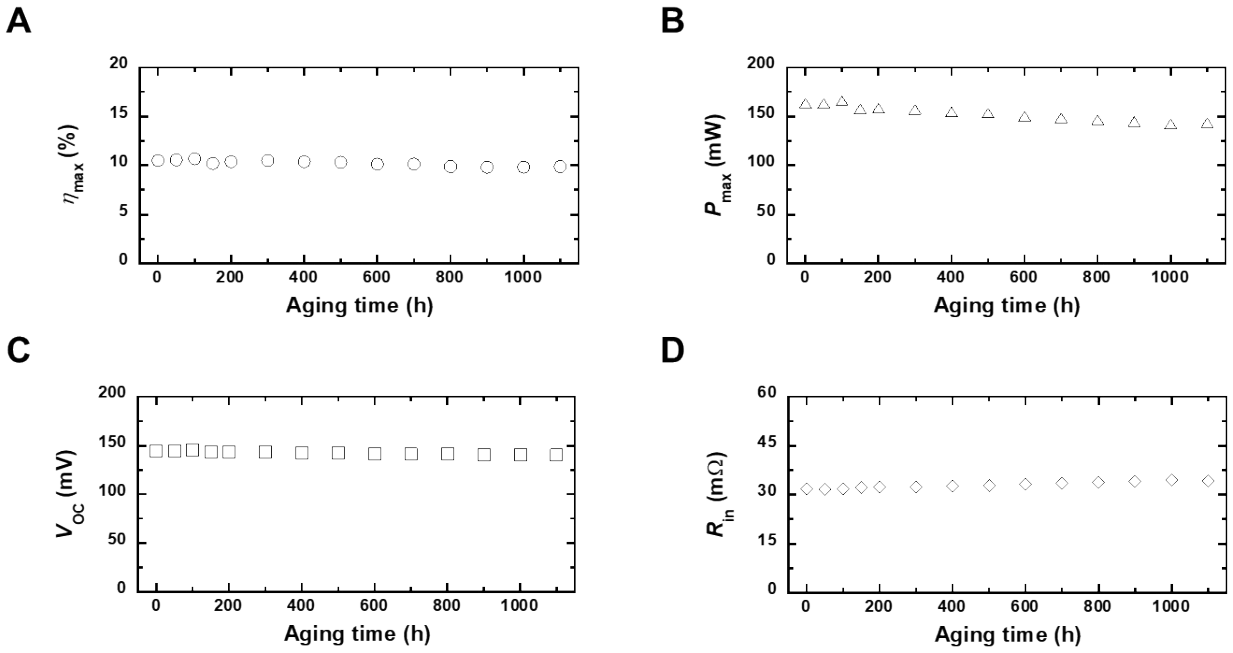

Figure S12. Aging test results of CZTSSe-based single-leg at 800 K for confirming thermal stability. Stable (**A**) open-circuit voltage (V_{OC}), (**B**) internal resistance (R_{in}), (**C**) maximum output power (P_{max}), and (**D**) maximum efficiency (η_{max}).

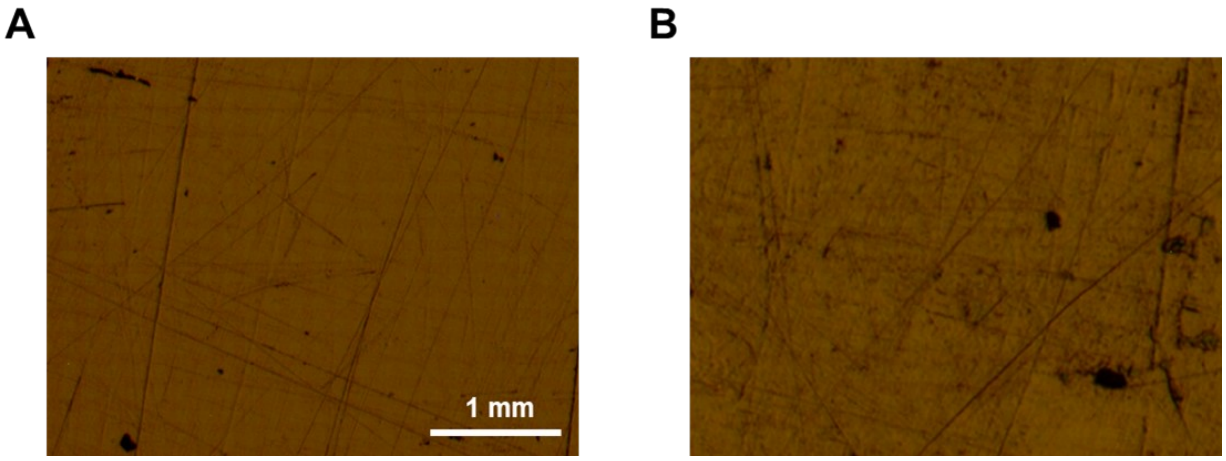

Figure S13. The optical surface images of CZTSSe single-leg device (**A**) before and (**B**) after aging test for 1100 h at 800 K.

Table S1. The detailed composition of $Cu_2ZnSn(S_{1-x}Se_x)_4$ samples determined by ICP-AES.

	x	K (mol%)	Cu (at.%)	Zn (at.%)	Sn (at.%)	S (at.%)	Se (at.%)
Sample 1	0.2	-	24.1	12.9	12.3	40.6	10.1
Sample 2	0.5	-	23.8	13.3	12.0	24.8	26.1
Sample 3	0.8	-	24.0	13.2	12.2	10.9	39.7
Sample 4	0.5	0.14	23.7	13.0	12.1	26.3	25.8
Sample 5	1.0	0.12	23.9	13.2	12.4	-	50.5

Table S2. Unintentional impurity levels detected by ICP-AES in the CZTSSe smples.

Impurity (ppb)	Sample 1	Sample 2	Sample 3	Sample 4	Sample 5
C	610	530	430	410	550
N	40	20	35	45	25
O	340	320	290	270	330
Mg	710	510	490	520	430
Al	300	280	250	250	190
Si	200	250	410	260	310
Ni	50	40	45	65	45
Fe	25	25	35	50	50

Table S3. Results Hall effect measurement and electrical conduction parameters for CZTSSe samples determined as described in the main text.

	Electrical properties at 300 K			Conduction parameters	
	p (cm^{-3})	σ (S/cm)	μ (cm^2/Vs)	σ_B (S/cm)	E_A (meV)
Sample 1	5.2×10^{17}	13.2	158.6	265	75
Sample 2	2.0×10^{18}	41.1	127.8	273	52
Sample 3	2.2×10^{18}	66.2	186.4	298	40
Sample 4	7.4×10^{18}	146.4	123.6	360	23
Sample 5	2.6×10^{19}	323.7	77.8	-	-

Table S4. The parameters for the Callaway model calculation.

	CZTS	CZTSe	Method	Reference
a (Å)	5.455	5.692	Exp.	This study
c (Å)	10.881	11.434	Exp.	This study
θ_D (K)	302	228	Exp.	This study
v_m (m/s)	3360	2455	Cal.	S12
κ_{L0} (W/mK)	4.29	3.57	Exp.	This study
ε	125		Cal.	This study

Table S5. High temperature TE properties of CZTSSe single crystal compared to some relating quaternary materials.

Material	σ (S/cm)	S (μV/K)	PF (10^{-3}W/mK^2)	κ (W/mK)	ZT	T_{ZT} (K)	Ref.
Sample 4	231	309	2.21	0.93	1.9	800	This work
$Cu_{2.125}Zn_{0.875}SnS_4$	197	153	0.46	0.31	1.07	723	S13
$Cu_{2.19}Zn_{0.8}Sn_{0.75}S_{3.53}$	14	301	0.125	0.645	0.14	700	S14
$Cu_2ZnSn_{0.9}In_{0.1}Se_4$	102	300	0.92	0.82	0.95	850	S15
$Cu_{2.2}Zn_{0.8}SnSe_4$	157	192	0.58	0.54	0.86	800	S16
$Cu_{2.15}Cd_{0.85}SnSe_{3.9}$	67	180	0.22	0.21	0.71	685	S17
$Cu_2CoSnSe_4$	130	230	0.69	0.84	0.7	850	S18
$Cu_{2.15}Zn_{0.85}GeSe_{3.9}$	206	120	0.30	0.4	0.55	723	S19
$Cu_2MnSnSe_4$	52	270	0.37	0.6	0.52	850	S18
$Cu_2Zn_{0.4}Fe_{0.6}SnSe_4$	75	232	0.40	0.7	0.46	800	S20
$Cu_2FeSnSe_4$	64	235	0.35	0.75	0.4	850	S18
$Cu_{2.075}Co_{0.925}GeS_4$	90	242	0.52	0.93	0.37	725	S21
$Cu_{2.3}Hg_{0.7}SnSe_{3.8}$	66	158	0.16	0.55	0.2	723	S22

Supplementary References

S1. I. D. Olekseyuk, I. V. Dudchak, and L. V. Piskach, J. Alloys Compd. **368**, 135 (2004).

S2. I. V. Dudchak, and L. V. Piskach, J. Alloys Compd. **351**, 145 (2003).

S3. A. Nagaoka, K. Yoshino, H. Taniguchi, T. Taniyama, and H. Miyake, J. Crystal Growth **341**, 38 (2012).

S4. A. Nagaoka, R. Katsube, S. Nakatsuka, K. Yoshino, T. Taniyama, H. Miyake, K. Kakimoto, M. A. Scarpulla, and Y. Nose, J. Crystal Growth **423**, 9 (2015).

S5. A. Nagaoka, K. Yoshino, T. Masuda, T. D. Sparks, M. A. Scarpulla, and K. Nishioka, J. Mater. Chem. A **9**, 15595 (2021).

S6. M. Dimitrievska, H. Xie, A. Fairbrother, X. Fontané, G. Gurieva, E. Saucedo, A. Pérez-Rodríguez, S. Schorr, and V. Izquierdo-Roca, Appl. Phys. Lett. **105**, 031913 (2014).

S7. E. Isotta, B. Mukherjee, C. Fanciulli, N. M. Pugno, and P. Scardi, J. Phys. Chem. C **124**, 7091 (2020).

S8. H. Hempel, R. Eichberger, I. Repins, and T. Unold, Thin Solid Films **666**, 40 (2018).

S9. H. Zhu, R. He, J. Mao, Q. Zhu, C. Li, J. Sun, W. Ren, Y. Wang, Z. Liu, Z. Tang, A. Sotnikov, Z. Wang, D. Broido, D. J. Singh, G. Chen, K. Nielsch, and Z. Ren, Nat. Commun. **9**, 2497 (2018).

S10. C. Xu, Z. Liang, H. Shang, D. Wang, H. Wang, F. Ding, J. Mao, and Z. Ren, Mater. Today Phys. **17**, 100336 (2021).

S11. Q. Zhu, S. Song, H. Zhu, and Z. Ren, J. Power Sources **414**, 393 (2019).

S12. S. Bensalem, M. Chegaar, D. Maouche, and A. Bouhemadou, J. Alloys Compd. **589**, 137 (2014).

S13. Q. Jiang, H. Yan, Y. Lin, Y. Shen, J. Yang, and M. J. Reece, J. Mater. Chem. A **8**, 10909 (2020).

S14. H. Yang, L. A. Jauregui, G. Zhang, Y. P. Chen, and Y. Wu, Nano Lett. **12**, 540 (2012).

S15. X. Y. Shi, F. Q. Huang, M. L. Liu, and L. D. Chen, Appl. Phys. Lett. **94**, 122103 (2009).

S16. Y. Dong, H. Wang, and G. S. Nolas, Phys. Status Solidi RRL **8**, 61 (2014).

S17. M. Ibáñez, D. Cadavid, R. Zamani, N. G. -Castelló, V. I. -Roca, W. Li, A. Fairbrother, J. D. Prades, A. Shavel, J. Arbiol, A. P. -Rodríguez, J. R. Morante, and A. Cabot, Chem. Mater. **24**, 562 (2012).

S18. Q. Song, P. Qiu, F. Hao, K. Zhao, T. Zhang, D. Ren, X. Shi, and L. Chen, Adv. Electron. Mater. **2**, 1600312 (2016).

S19. M. Ibáñez, R. Zamani, A. LaLonde, D. Cadavid, W. Lin, A. Shavel, J. Arbiol, J. R. Morante, S. Gorsse, G. J. Snyder, and A. Cabot, J. Am. Chem. Soc. **134**, 4060 (2012).

S20. Y. Dong, H. Wang, and G. S. Nolas, Inorg. Chem. **52**, 14364 (2013).

S21. C. Bourgès, R. Al Rahal Al Orabi, and Y. Miyazaki, J. Alloys Compd. **826**, 154240 (2020).

S22. W. Li, M. Ibáñez, R. R. Zamani, N. G. -Castelló, S. Gorsse, D. Cadavid, J. D. Prades, J. Arbiol, and A. Cabot, CrystEngComm **15**, 8966 (2013).